Recent Results from ZEUS*

Brian Foster†

H.H. Wills Physics Laboratory
University of Bristol, Bristol, BS8 1TL, UK

On behalf of the ZEUS collaboration

Abstract

Recent results on deep inelastic scattering from the ZEUS collaboration are reviewed. These include studies of neutral and charged currents at high Q^2, fragmentation and perturbative QCD, and information on the quark and gluon content of the proton. Information on the gluon density in the proton is obtained from a wide variety of processes, leading to a consistent picture of a steep rise of the gluon density at low x. Preliminary measurements of F_2 extending to new regimes at both high and low Q^2 and x are presented based on 1994 data. Analysis of events with a large rapidity gap with respect to the direction of the proton beam is consistent with factorisation of the cross-section into a flux factor and a structure function, and can be interpreted as an indication of point-like constituents inside the pomeron.

1. Introduction

Historically, deep inelastic scattering of leptons from the proton has been a vital probe of the proton's structure and of the nature of the strong and electroweak forces. This tradition continues at HERA, where access to unprecedented ranges in Q^2 and x has resulted in a wealth of new information. In this talk I will give an overview of recent results from the ZEUS experiment. Many of the topics I will address are covered in much greater detail in contributions to parallel sessions at this conference. The H1 collaboration also have data on many on the topics covered here; rather than giving explicit references, I refer the reader to the contribution of J. Dainton in these proceedings, in which a full bibliography of the H1 results may be found.

† Supported by PPARC; E-mail *bf@siva.bris.ac.uk*

* Talk given in the plenary session at the Workshop on Deep Inelastic scattering and QCD, Paris, April 1995.

2. High Q^2 Neutral and Charged Current processes

HERA provides a unique opportunity to study the electroweak interaction at Q^2 sufficiently high that the charged and weak currents are of similar strength. Equation (1) shows the general form for the differential cross-section in terms of the structure functions $\mathcal{F}_1$, $\mathcal{F}_2$ and $\mathcal{F}_3$.

$$\frac{d^2\sigma}{dxdQ^2} = \frac{2\pi\alpha^2}{xQ^4}\left[2xy^2\mathcal{F}_1 + 2(1-y)\mathcal{F}_2 + \{1-(1-y)^2\}x\mathcal{F}_3\right] \quad (1)$$

The structure functions are products of quark distribution functions and the couplings of the currents mediating the interaction.

At high Q^2 both charged and neutral current processes can be clearly identified and separated from

backgrounds. Neutral current processes can be isolated by identifying the high-energy scattered charged lepton in the Uranium-scintillator calorimeter [1]. In charged current events the fact that the outgoing and undetected ν carries away a large amount of $p_{\rm T}$ means that these events can be cleanly isolated in most regions of phase space. Figure 1 shows the differential cross-section for the charged and neutral currents as a function of Q^2. It can be seen that these two processes become of equal strength at $Q^2 \sim 10^4$ GeV^2. Furthermore the data clearly exclude an infinite mass W and allow a determination of the W mass to be $M_W = 76 \pm 16 \pm 13$ GeV, in good agreement with the world average of 80.22 ± 0.26 GeV.

Information on the Standard Model can also be obtained by looking at the ratio of the neutral current and charged current cross-sections as a function of Q^2. The fact that the charged current cross-sections behave differently as a function of Q^2 can be seen from the approximate relations derived from (1) and shown in equations (2), (3)

$$\left.\frac{d^2\sigma}{dxdQ^2}\right|_{e^-} = \frac{G_F^2}{2\pi}\left(\frac{M_W^2}{M_W^2+Q^2}\right)^2 2x\cos^2\theta_c \cdot\{u + c + (1-y)^2(\overline{d}+\overline{s})\} \qquad (2)$$

$$\left.\frac{d^2\sigma}{dxdQ^2}\right|_{e^+} = \frac{G_F^2}{2\pi}\left(\frac{M_W^2}{M_W^2+Q^2}\right)^2 2x\cos^2\theta_c \cdot\{\overline{u} + \overline{c} + (1-y)^2(d+s)\} \qquad (3)$$

Since at high Q^2 both $x, y \to 1$, quarks dominate the cross-section in the case of electrons and sea antiquarks in the case of positrons. Since the density of sea quarks tends to 0 as $x \to 1$, the ratio of positron to electron cross-sections will fall to 0. This behaviour is shown in Figure 2, together with the ratio for neutral currents, which also falls as Q^2 increases. Within large statistical errors, the data is consistent with the Standard Model prediction. Clearly this area of ZEUS physics will benefit from much more luminosity. In particular, substantially more running with electrons is required to reduce the errors on the cross-section ratios.

3. Properties of the Strong Interaction

The large increase in centre of mass energy at HERA greatly improves the sensitivity of studies in perturbative and non-perturbative aspects of QCD compared to fixed target experiments.

3.1. Inclusive charged particle distributions

The charged particle distributions in neutral current deep inelastic scattering are sensitive both to the hadronisation process and to the underlying QCD processes at the parton level. It is usual to study charged particle distributions in variables aligned with the exchanged virtual photon; the fractional momentum along the virtual photon direction known as the Feynman variable, $x_{\rm F}$, and the momentum perpendicular to the virtual photon, $p_{\rm T}^\star$. Charged tracks in ZEUS are reconstructed principally using the Central Tracking Detector (CTD) [2]. In order to keep within the well-understood and high-acceptance region of this detector, only those charged particles with $p_{\rm T} > 0.2$ GeV and $25^o < \theta < 155^o$, where θ is the polar angle, are analysed. This restricts the range in Q^2 and W to $10 < Q^2 < 160$ GeV^2 and $75 < W < 175$ GeV.

Figure 3 shows the normalised $x_{\rm F}$ distribution for deep inelastic scattering events, excluding those with a large rapidity gap in the forward direction indicative of a diffractive type interaction. The ZEUS data are shown together with e^+e^- data from the DELPHI experiment [3] at a similar mean W. It can be seen that the ZEUS and e^+e^- data are in good agreement with each other and with the solid line which is the prediction of the MEPS model. Lower energy data from μ p scattering (not shown) is consistent with the quark-parton model prediction.

Figure 4 shows $< p_{\rm T}^{\star 2} >$ as a function of W for different ranges of $x_{\rm F}$. The ZEUS data agree well with the predictions of the MEPS model, shown as a solid line, and show a much steeper rise in $< p_{\rm T}^{\star 2} >$ than the fixed target data for a similar range in W. Figure 5 shows that $< p_{\rm T}^{\star 2} >$ for the ZEUS data increases strongly with Q^2, in contrast with the EMC data which show almost no rise over a similar range of Q^2. Thus for the first time the expected rise in $< p_{\rm T}^{\star 2} >$ due to hard gluon radiation can be seen in deep inelastic scattering data.

3.2. Determination of α_s from jet multiplicity

At high Q^2 the strongly accelerated struck quark from the proton can radiate hard gluons which may lead to resolvable jets in the final state. The rate of jet production is proportional to the value of the strong coupling constant, α_s. Jets are found using the JADE jet algorithm [7]. The rate of events containing two identifiable jets together with the forward jet resulting from the breakup of the proton (2 + 1 jet events) is compared with the rate expected in a Monte Carlo model including next to leading order QCD effects. The effect of hadronisation on this rate is large and varies depending on the exact criteria used in defining a jet. In order to reduce uncertainties in the hadronisation process and to avoid the very forward region which is not well modelled, the following cuts on the kinematic variables were made: $0.1 < y < 0.95$, $0.01 < x < 0.1$ and $120 < Q^2 < 3600$ GeV^2. Good agreement is obtained

between the Monte Carlo and the data in this kinematic region. A cut on the variable which defines when jets can be resolved, $y_{cut} < 0.02$, was used in order to determine α_s.

Three bins of Q^2 were used in the analysis. The resultant α_s values shown in Figure 6 indicate a variation with Q. Averaged over the full Q^2 range and evolving to $Q^2 = M_Z^2$, ZEUS data gives

$$\alpha_s(M_Z) = 0.117 \pm 0.005(stat.)^{+0.008}_{-0.009}(syst.) \qquad (4)$$

where the systematic error includes the experimental and theoretical errors added in quadrature.

3.3. Transverse energy flow in the forward direction

The new kinematic region opened up by HERA has led to a great deal of theoretical interest in the appropriate QCD dynamical prescription at very low x. The standard DGLAP [8] approach imposes a "strong ordering" in the transverse momentum of the gluons emitted between the struck quark, or "current" jet, and the proton remnant, such that gluons emitted near to the current jet direction have much larger p_T than those emitted close to the proton direction. In contrast, the BFKL [9] approach has no such ordering in transverse momenta. Thus one might qualitatively expect that, in a region in which the BFKL approach was appropriate, there would be an excess of transverse energy in the proton direction compared to the prediction of a DGLAP based model. In particular, BFKL dynamics would predict that the average level of transverse energy per unit pseudorapidity η ($\eta = -\ln(\tan\theta/2)$) in the forward direction would grow as x^{-1}.

Unfortunately, experimentally the forward direction is very complex and difficult to understand. The energy observed in the ZEUS calorimeter as a function of η is strongly affected by scattering from the beam pipe, accelerator elements, inactive material between calorimeter cells etc. A careful Monte Carlo study is therefore required to unfold the true energy flow. The corrected energy flow resulting from such a study is shown in Figure 7 in various bins of $< Q^2 >$ and $< x >$. Also shown in the figure are the predictions of the CDMBGF model [10] and the MEPS model [4]. The most striking characteristic of the data is the long tail of high transverse energy at high η, i.e. in the forward (proton) direction, which becomes increasingly marked as x falls, independent of Q^2, qualitatively in agreement with the expectations of BFKL dynamics. Up to $\eta \sim 4$ the transverse energy flow is about 2 GeV/unit rapidity, in reasonably good agreement with the CDMBGF model, but not with the MEPS model. However, neither model explains all aspects of the data and in particular both fail to describe the current jet region in rapidity at low Q^2 and low x. More data in a wider kinematic region will be required before any conclusions as to the appropriate QCD dynamics in this region can be drawn.

4. The constituents of the proton

In this section the various methods of extracting information on the gluon structure function are outlined. These are based predominantly on the analysis of ZEUS data taken in 1993. Preliminary results on the quark densities inside the proton are given from the determination of the F_2 structure function using 1994 data. The 1994 data allow an extension of the kinematic range which can be measured, to lower Q^2 by means of a dedicated run with a vertex shifted away from the nominal interaction point, and at high Q^2 by a large increase in the integrated luminosity collected by ZEUS in 1994.

4.1. Gluon structure function

A variety of different methods can now be used to estimate the gluon structure function of the proton. The "classic" way of measuring $G(x)(= xg(x))$ is to measure the scaling violations in F_2 as a function of Q^2. Other processes can give information, although usually in a rather more model dependent way. The measurement of inclusive charm production in photoproduction and of vector meson production in both photoproduction and deep inelastic scattering can also provide information on $G(x)$.

4.1.1. $G(x)$ from scaling violations in F_2 The ZEUS analysis of scaling violations on 1993 data has already been published [11]. Figure 8 shows the results of this analysis. Two methods using approximations to the QCD evolution equations to extract $G(x)$ in bins of x are shown, due to Prytz [12], and Ellis, Kunszt and Levin [13]. Also shown is the result of a full next to leading order QCD fit based on DGLAP evolution of the F_2 structure function. It can be seen that approximate methods are consistent with the full QCD fit, which in turn matches well to a determination of $G(x)$ by NMC [14]. This measurement extends our knowledge of $G(x)$ by almost two orders of magnitude in x and remains the least model-dependent method to determine it.

4.1.2. Charm cross-section in photoproduction The dominant mechanism for production of charm-anticharm quark pairs at HERA is photon-gluon fusion. The gluon from the proton can split into a $c\bar{c}$ pair which interacts either directly with the virtual photon or with a constituent of the photon in a so-called "resolved photon" interaction. In either case the cross-section for charm

production depends on the probability of finding a gluon in the proton and therefore measurement of this cross-section in principle allows an unfolding of $G(x)$.

Two distinct methods which isolate charm production have been used. The first uses the decay $D^\star \to D\pi_s \to K\pi\pi$, where the π_s is restricted to a very small area of phase space just above threshold. This produces a signal in the mass difference between the $K\pi\pi$ and $K\pi$ combinations which can be cut on to produce a clear D signal [16]. The other method uses high $p_{\rm T}$ leptons, in this case muons, as a signal for inclusive charm production. Figure 9 shows the cross-sections obtained from these signals as a function of W, together with low energy data from fixed target experiments [17]. The solid curve shows the predictions of a next to leading order QCD model by Frixone et al [20], using as input the proton structure function parameterisation of $MRSD'_$ [15] and the photon structure prediction due to Glück, Reya and Vogt [18]. The dotted lines on either side of the solid line show the variation in the cross-section obtained using alternative parameterisations which are broadly compatible with the data on photon and proton structure functions. The size of these variations and the fact that they depend on the photon structure as well as the proton structure imply that much more data will be necessary before this method can lead to an accurate determination of the gluon density in the proton.

4.1.3. Vector meson production Some perturbative QCD models of vector meson production [21] [22] consider it to proceed via the colour singlet exchange of two gluons, thereby in principle increasing the sensitivity to the gluon density. However, the extraction of the gluon distribution does rely on explicit theoretical assumptions which currently cannot be well motivated from data.

One particularly clean channel is elastic J/ψ production. Pairs of oppositely charged leptons, either with well reconstructed charged tracks matching energy deposits in the calorimeter consistent with e^+ or e^- or with charged tracks pointing to hits in the muon chambers consistent with μ^+ or μ^-, are selected from events with no other activity in the ZEUS detector. The effective mass of the leptons shows a clear peak at the J/ψ mass with very little background. The total $\gamma^\star p$ cross-section obtained from these signals can be plotted as a function of W. ZEUS data from 1993 have been published [23], which, in conjunction with data from fixed target experiments showed that the J/ψ cross-section was rising quickly with W, much faster than would be predicted from models based on vector meson dominance or Regge theory. Preliminary analysis of the 1994 data allows a similar conclusion to be drawn from ZEUS data alone, as can be seen in Figure 10.

Another channel sensitive to the gluon distribution is the production of ρ and other vector mesons at $Q^2 \neq 0$. In the model of Brodsky et al. [22] the cross-section of vector mesons produced by longitudinally polarized photons is proportional to the square of the gluon density in the proton. The data selection for deep inelastic vector meson production is straight-forward. Two charged tracks consistent with being hadrons and a scattered positron indicative of deep inelastic scattering are required. Kinematic cuts are used to reduce the photoproduction background caused by the misidentification of energy deposits in the calorimeter as a scattered positron. The signal obtained is shown in Figure 11, where a clear ρ signal with the expected mass and width is observed with very little background. The $\gamma^\star p$ cross-section for ρ is shown in Figure 12. The ZEUS measurement for the gluon distribution from the F_2 scaling violations can be used within the framework of the model of Brodsky et al. to obtain a prediction which is also shown in Figure 12. It can be seen that, within the present statistics, the ZEUS data is consistent with the Brodsky model and inconsistent with a 'soft' Pomeron exchange [26].

The above data demonstrate that a consistent picture is emerging for the gluon density using a variety of different methods, including the "classic" method of scaling violations in DIS. At the moment however, the other methods are really only consistency checks. A better understanding of the theoretical uncertainties and more precise data are required before a measurement of $G(x)$ can be obtained from inclusive charm and vector meson production.

4.2. The quark distributions in the proton

For neutral current deep inelastic scattering and for $Q^2 \ll M_Z^2$, only the parity-conserving structure functions $\mathcal{F}_1$ and $\mathcal{F}_2$ from equation (1) need be considered, the contribution from Z^0 exchange can be neglected and defining the longitudinal structure function, $F_{\rm L}$, as $F_{\rm L} = F_2 - 2xF_1$ gives

$$\frac{d^2\sigma}{dxdQ^2} = \frac{2\pi\alpha^2}{xQ^4}\left[\{1+(1-y)^2\}F_2(x,Q^2) - y^2F_{\rm L}\right](1+\delta_r(x,Q^2)) \qquad (5)$$

where δ_r contains the corrections due to electroweak radiative effects. Since we are currently not able to determine $F_{\rm L}$, its value is taken from the QCD prescription using the MRSA [27] parton distributions. In the region of phase space used in the F_2 analysis the correction due to $F_{\rm L}$ is small.

ZEUS has already published F_2 as determined from the data taken in 1993 [28]. In 1994 three factors improved the quality of the ZEUS F_2 measurement. First, a factor of ~ 6 more data was collected. Secondly, improvements in the instrumentation of

ZEUS, particularly in the rear direction close to the beam pipe, expanded the angular range in which scattered positrons could be measured. Thirdly, some special runs were taken with the vertex displaced by about 67 cm in the proton direction. This means that positrons scattered at smaller angles, and hence lower Q^2, can be accepted for the F_2 analysis.

In order to determine F_2 it is essential to have a detailed understanding of the ZEUS detector and possible systematic effects. DIS can be fully described in terms of two independent variables, most commonly x and Q^2. Owing to the hermetic nature of the ZEUS detector, x and Q^2 can be determined from measurements of the scattered positron, of the hadronic system, or a combination of the two. In ZEUS the so-called "Double Angle" (DA) method, which uses the angles of the scattered lepton and current jet, and the "Electron" method, which uses the energy and angle of the scattered lepton, are preferred. The determination of F_2 uses both these methods, which give a good systematic check of the analysis procedure. The data are binned in x, Q^2 with bin sizes determined by detector resolution, statistics, migration in and out of the bin due to the finite resolution of ZEUS etc. The data are corrected for acceptance and migration via Monte Carlo simulation. Multiplying by the appropriate kinematic and correction factors shown in equation (5) gives values of F_2 in the chosen bins.

We first discuss the results from the 58 nb^{-1} of data taken with a shifted vertex. The shifted vertex together with the improvement of the instrumentation in the rear direction mean that we can now analyse down to $Q^2 \sim 2$ GeV^2, compared to $Q^2 \sim 8.5$ GeV^2 for the 1993 data. The energy and angle of the scattered electron give better resolution than the Double Angle method at low Q^2 and the Electron method has therefore been used in this analysis. Figure 13 shows the results for Q^2 bins between 2 and 15 GeV^2. Also shown are parameterisations of F_2 from various theoretical groups.

The large increase in data taken and the improvement in the instrumentation in the rear direction have also resulted in an increase in the range of (x, Q^2) for the data taken at the nominal interaction point. More bins have been used in the analysis and the Q^2 reach has increased to $Q^2 = 5000$ GeV^2. Figure 14 shows the results for F_2 with DA variables for the lower Q^2 bins. Good agreement is seen with the NLO QCD fit to the ZEUS 1993 data.

Figure 15 shows the value of F_2 converted to a total virtual photon-proton cross-section plotted against W^2 for various Q^2 values. Also shown is the total photoproduction cross-section as measured by ZEUS, together with data at various values of Q^2 from fixed target experiments. The striking feature of this plot is that the steeply rising cross-section as a function of W^2 ($W^2 \sim Q^2/x$) seen at high values of Q^2 persists down to the lowest value of Q^2 so far measured. However, as shown by the solid lines in Figure 15, at $Q^2 = 0$ the rise is much less steep and is well represented by models using a 'soft' prescription based on Regge theory. There must be a transition between this steeply rising cross-section and the shallower rise in photoproduction, but so far there is no sign of this.

5. The pomeron content of the proton and the structure of the pomeron

5.1. Deep Inelastic scattering measurements

In most deep inelastic scattering events at HERA, the proton breaks up after the scatter. This leads to a large energy deposit around those sections of the calorimeter closest to the beam pipe in the incident proton direction. However, it was observed in 1993 [35] that $\sim 10\%$ of DIS events did not show such a forward energy deposit and instead were characterised by a "large rapidity gap" between the first substantial energy deposit in the calorimeter and the incident proton direction. Similar events have also been observed in proton-proton collisions [36]. The most natural interpretation of such events is that they correspond to diffractive scattering of the virtual photon from the proton, leaving the proton intact and able to leave the interaction undetected inside the beam pipe. Since diffraction is normally considered to proceed by the exchange of a colourless particle with the quantum numbers of the vacuum known as the pomeron [37], the study of such events can in principle give information on the flux of pomerons in the proton and on the structure of the pomeron itself.

The event selection is based on cuts in the maximum pseudorapidity, $\eta_{\max}$, defined as the pseudorapidity of the most forward energy deposit in the calorimeter above a given threshold, and $\cos\theta_H$, the energy weighted direction of hadronic activity in the calorimeter, defined as $\cos\theta_H = \frac{\sum_i p_{z_i}}{|\sum_i \vec{p_i}|}$. Figure 16 shows the data together with two Monte Carlo models used to describe non-diffractive and diffractive samples in DIS. It can be seen that the non-diffractive sample is concentrated at low θ_H and high $\eta_{\max}$ and that the diffractive events can be isolated by selecting $\eta_{\max} < 2.5$ and $\cos\theta_H < 0.75$.

The clean sample of diffractive events isolated by the above cuts can be analysed under the assumption that the reaction proceeds via pomeron exchange. The kinematic variables are illustrated in Figure 17 where

$$
\begin{aligned}
t &= (p-p')^2 \simeq 0 \\
x_{I\!P} &= \frac{(p-p')\cdot q}{p\cdot q} \simeq \frac{M_X^2+Q^2}{W^2+Q^2} \simeq x_{IP/p} \qquad (6)\\
\beta &= \frac{x}{x_{I\!P}} \simeq \frac{Q^2}{M_X^2+Q^2} \simeq x_{q/IP}
\end{aligned}
$$

In analogy to the definition of the F_2 structure function of (1) it is possible to define a structure function for diffractive events, F_2^D, which in general depends on t, Q^2, β and $x_{I\!P}$. However, since the final state proton is undetected, the cross-section must be integrated over t to give

$$
\frac{d^3\sigma_{diff}}{dQ^2 d\beta dx_{I\!P}} = \frac{2\pi\alpha^2}{\beta Q^4}\,(1+(1-y)^2)\,F_2^{D(3)}(Q^2,\beta,x_{I\!P}) \quad (7)
$$

where the effects of a possible diffractive longitudinal structure function and radiative corrections have been ignored. Finally a further simplification is introduced which corresponds to the assumption that the pomeron has a structure which is independent of how it is produced and that the flux of pomerons inside the proton is independent of the process in which the pomeron takes part. This so-called "factorisation" allows $F_2^{D(3)}$ to be written as

$$
F_2^{D(3)} = f(x_{I\!P})\cdot F_2^{IP}(\beta,Q^2) \qquad (8)
$$

In order to extract from the data the relative normalisation of diffractive and non-diffractive events, fits were performed to the $\eta_{\max}$ and θ_H distributions using the CDMBGF model to describe the non-diffractive events and the POMPYT [39] implementation of the Ingelman-Schlein [40] model or an implementation [41] of the Nikolaev-Zacharov [38] model† to describe the diffractive events. Those fits giving acceptable χ^2 per degree of freedom imply a diffractive contribution ranging from 10 - 15 % . A model containing only a "soft" pomeron, i.e. where $F_2^{IP}(\beta)\sim(1-\beta)^5$, can be ruled out merely on the χ^2 of this fit. Thus from very general properties of the data the pomeron is required to have a hard component i.e. $F_2^{IP}(\beta)\sim\beta(1-\beta)$.

The general features of the data are well described by the MC models, allowing us to calculate the corrected differential cross-section and hence $F_2^{D(3)}$ in the kinematic regions where data, backgrounds and corrections are well understood. Figure 18 shows $F_2^{D(3)}$ as a function of $x_{I\!P}$ in bins of Q^2 and β. The data fall off steeply with increasing $x_{I\!P}$. If the factorisation assumption of equation (8) holds, then the data should follow a universal function of $x_{I\!P}$. A fit to the form

$$
F_2^{D(3)} \propto b_i\cdot(1/x_{I\!P})^a
$$

† Note that the NZ model is not factorisable.

where b_i were allowed to vary from bin to bin was found to give an acceptable fit with a universal slope of $a = 1.30 \pm 0.08(stat.)^{+0.08}_{-0.14}(syst.)$. Thus the data are consistent with factorisation, although they do not rule out non-factorisable models such as the NZ model. The solid lines in Figure 18 show a fit to a functional form, motivated by the theoretical models, of

$$
(1/x_{I\!P})^a\cdot b\cdot(\beta(1-\beta)+c/2\cdot(1-\beta)^2) \qquad (9)
$$

where a, b and c are constants. This gives an acceptable χ^2 per degree of freedom, whereas omitting the $(1-\beta)^2$ term produces an unacceptable fit.

Figure 19 shows $\tilde{F}_2^D$, the integral of $F_2^{D(3)}$ over the $x_{I\!P}$ range of $6.3\cdot10^{-4} < x_{I\!P} < 10^{-2}$. Binned in β, $\tilde{F}_2^D$ is approximately independent of Q^2, i.e. shows the scaling behaviour indicative of scattering from point-like partons inside the pomeron. Binned in Q^2, the data overshoot the hard pomeron prediction at low β implying that both hard and soft components of the pomeron are required. The data are also compatible with the Aligned Jet Model [42] which predicts a flat distribution in β.

On the assumption that the pomeron is a *bona-fide* particle it would be expected to satisfy a momentum sum rule, i.e. that the sum over the momentum distributions of its constituents should add up to its own momentum. All models with the normalisation set by the requirement of fulfilling the momentum sum rule from the light quarks alone lie substantially above the data, implying that if the pomeron is a real particle, its momentum must be carried by more than quark constituents.

5.2. Hard photoproduction measurements

The virtual photon in DIS couples only to electrically charged partons so that further information on a possible gluonic contribution to the pomeron structure must be obtained by other means. Fortunately HERA provides us with such a possibility via hard photoproduction. In a "resolved photon" process a gluon inside the photon may interact with a quark or gluon inside the pomeron.

A clear signal for diffractive-like events in hard photoproduction can be obtained from a sample of events containing jets in the final state. The cross-section for inclusive jet production where the most forward going hadron has $\eta_{\max} < 1.8$ measured in the range $-1 < \eta^{jet} < 1$ and $E_T^{jet} > 8$ GeV is shown in Figure 20. It can be seen that predictions from Monte Carlo models assuming the pomeron consists of soft gluons or hard quarks fall substantially below the data. Similarly the possible contribution from non-diffractive processes is too low and also has the wrong shape. The

hard gluon parameterisation of the pomeron however gives a good representation of the data.

The cross-section was compared to predictions from the POMPYT Monte Carlo using the Donnachie-Landshoff [44] flux factor and allowing for a mixture of hard gluons and quarks in the pomeron, together with some non-diffractive background. $\Sigma_{I\!P}$ is a free parameter in these fits and is defined as the sum of the pomeron constituents such that if the momentum sum rule is satisfied $\Sigma_{I\!P} = 1$. If we assume that the pomeron contains a fraction c_g of gluons, then for each value of c_g a fit can be made to the cross-sections varying $\Sigma_{I\!P}$. The results are shown in Figure 21. For $c_g = 0$, $\Sigma_{I\!P} = 2.5 \pm 0.9$, whereas for $c_g = 1$, $\Sigma_{I\!P} = 0.5 \pm 0.2$.

On the assumption that the parton densities in the pomeron are universal, we can combine the results from the hard photoproduction and DIS data. Defining $\Sigma_{I\!Pq}$ as the contribution to $\Sigma_{I\!P}$ coming from the quarks,

$$\int_{x_{I\!P\,min}}^{x_{I\!P\,max}} dx_{I\!P} \int_0^1 d\beta \; F_2^{D(3)}(\beta, Q^2, x_{I\!P}) = k_f \cdot \Sigma_{I\!Pq}(Q^2) \cdot I_{flux} \qquad (10)$$

where I_{flux} is the integral of the pomeron flux factor over t and k_f is either $5/18$ if u, d quarks contribute or $2/9$ if u, d, s contribute. Equation (10) can be evaluated using the measured $F_2^{D(3)}$ to give $\Sigma_{I\!Pq} = 0.32 \pm 0.05$ assuming two flavours or 0.40 ± 0.07 for three flavours and is also plotted in Figure 21.

Taking into account the statistical errors, the result for $\Sigma_{I\!P}$, $0.5 < \Sigma_{I\!P} < 1.1$ indicates that the data are consistent with the momentum sum rule for the pomeron being satisfied. Taking also into account those systematic errors which do not cancel in this comparison, the data indicate that $1/3$ of the momentum of the pomeron is carried by quarks and $2/3$ by gluons. Furthermore, the fraction of gluons inside the pomeron can be limited to $0.3 < c_g < 0.8$ at the 1σ level, independent both of the validity of the momentum sum rule and of the definition of the flux factor, provided that it is identical in photoproduction and DIS.

6. Summary and conclusions

It is clear that HERA is producing a wealth of physics results in deep inelastic scattering. Many studies in fragmentation, non-perturbative QCD and perturbative QCD dynamics have only been touched on briefly in this talk. The measurement of F_2 of the proton is becoming increasingly precise and is being carried out in an ever larger area of the Q^2- x plane. At low Q^2 we still see no evidence for the transition from a steeply rising structure function to the shallower rise implied by the cross-section data for real photon interactions. This transition region seems to be below $Q^2 = 2$ GeV^2, a figure which implies that when it occurs it must be relatively sudden and therefore interesting. In order to be better able to study this phenomenon, ZEUS has added a Beam Pipe Calorimeter in the rear direction which should extend the precise measurement of F_2 down to $Q^2 \sim 0.2$ GeV^2. At high Q^2, increasing luminosity has resulted in sensitivity to the Standard Model predictions for the relative strengths of the charged and neutral weak currents. The increase in both the precision and range of the F_2 measurement leads to better determination of the gluon density. Several alternative measurements of this are now possible and will provide valuable consistency checks on both the experimental methods and the theoretical framework. The status of diffractive phenomena in deep inelastic scattering is rather reminiscent of that of F_2 in the '60's and '70's at SLAC. The first indications of point like partons inside the pomeron and a large gluonic content have been observed. ZEUS has installed a detector designed to explore new regions of phase space in diffractive phenomena. The Leading Proton Spectrometer can measure the diffractively scattered proton with excellent precision and was working well in the 1994 data taking. Preliminary analysis of data show that we are sensitive to much lower values of β and higher values of $x_{I\!P}$ than hitherto. Thus future prospects for ZEUS physics are very bright. The past few years have brought surprises such as the steep rise of F_2 at low x and the opening up of the investigation of diffractive phenomena. Surely many more surprises and excitement are in store.

Acknowledgements

It is a pleasure to acknowledge many useful discussions with my colleagues on ZEUS. I am particularly grateful to R. Devenish, R. Klanner, M. Lancaster and A. Levy for their comments on the manuscript. I am also grateful to the organisers for a very enjoyable workshop in Paris.

References

[1] A. Andresen et al., Nucl. Instrum. Methods, A305 (1991) 101; A. Bernstein et al., Nucl. Instrum. Methods, A336 (1993) 23.
[2] N. Harnew et al., Nucl.Instrum. Methods, A279 (1989) 290; B. Foster et al., Nucl. Phys. B (Proc. Suppl.) 32 (1993) 181; B. Foster et al., Nucl. Instrum. Methods A338 (1994) 254.
[3] DELPHI Collab., P. Abreu et al., Phys. Lett. B311 (1993) 408.
[4] G. Ingelman, Proceedings of the Workshop on Physics at HERA, DESY Vol. 3 (1992) 1366;
M. Bengtsson, G. Ingelman, T. Sjöstrand, Nucl. Phys. B301 (1988) 554.
[5] EMC Collab., J. Ashman et al., Z. Phys. C52 (1991) 361.
[6] E665 Collab., M.R. Adams et al., Phys. Lett. B272 (1991) 163.

[7] JADE Collab., W. Bartel et al., Z. Phys. C33, (1986) 23; JADE Collab., S. Bethke et al., Phys. Lett. B213 (1988) 235.
[8] V.N. Gribov and L.N. Lipatov, Sov. J. Nucl. Phys. 15 (1972) 438, 675; L.N. Lipatov, Sov. J. Nucl. Phys. 20 (1975) 94; Yu. L. Dokshitzer, Sov. Phys. JETP 46 (1977) 641; G. Altarelli and G. Parisi, Nucl. Phys. B126 (1977) 298.
[9] E.A. Kuraev, L.N. Lipatov, and V.S. Fadin, Sov. Phys. JETP 45 (1977) 199; Y.Y. Balitsky and L.N. Lipatov, Sov. J. Nucl. Phys. 28 (1978) 822.
[10] T. Sjöstrand, Comp. Phys. Comm. 39 (1986) 347; T. Sjöstrand and M. Bengtsson, ibid. 43 (1987) 367.
[11] ZEUS Collab., M. Derrick et al., Phys. Lett. B345 (1995) 576.
[12] K. Prytz, Phys. Lett. B332 (1994) 393.
[13] R.K. Ellis, Z. Kunszt and E.M. Levin, Nucl. Phys. B420 (1994) 517.
[14] NMC Collab., M. Arneodo et al., Phys. Lett. B309 (1993) 222.
[15] A.D. Martin, W.J. Stirling and R.G. Roberts, Phys. Lett. B306 (1993) 145; Phys. Lett. B309 (1993) 492 (erratum).
[16] ZEUS Collab., M. Derrick et al., Phys. Lett. B349 (1995) 225.
[17] CIF Collab., M.S. Atiya et al., Phys. Rev. Lett 43 (1979) 414; BFP Collab., A.R. Clark et al., Phys. Rev. Lett. 45 (1980) 682; SLAC HFP Collab., K. Abe at al., Phys. Rev. D30 (1984) 1; EMC Collab., M. Arneodo et al., Z. Phys, C35 (1987) 1; PEC Collab., M. Adamovich et al., Phys. Lett. B187 (1987) 437; E691 Collab., J.C. Anjos et al., Phys. Rev. Lett. 65 (1990) 2503; NA-14′ Collab., M.P. Alvarez et al., Z. Phys. C60 (1993) 53.
[18] M. Glück, E. Reya and A. Vogt, Phys. Lett. B306 (1993) 391.
[19] H. Abramowicz, K. Charchula and A. Levy, Phys. Lett. B269 (1991) 458.
[20] S. Frixone, M.L. Mangano, P. Nason and G. Ridolfi (private communication); see also Nucl. Phys. B412 (1994) 225.
[21] M.G. Ryskin, Z. Phys. C57 (1993) 89; and private communication.
[22] S.J. Brodsky et al., Phys. Rev. D50 (1994) 3134.
[23] ZEUS Collab., M. Derrick et al., Phys. Lett. B350 (1995) 120-134
[24] A. Donnachie and P.V. Landshoff, Phys. Lett. B348 (1995) 213.
[25] NMC Collab., P. Amaudruz et al., Z. Phys. C54 (1992) 239; M. Arneodo et al., Nucl. Phys. B429 (1994) 503.
[26] A. Donnachie and P.V. Landshoff, Phys. Lett. B185 (1987) 403.
[27] A.D. Martin, R.G. Roberts and W.J. Stirling, Phys. Rev. D50 (1994) 6734.
[28] ZEUS Collab., M. Derrick et al., Z. Phys. C65 (1995) 379.
[29] A.D. Martin, R.G. Roberts and W.J. Stirling, Phys. Rev. D51 (1995) 4756; RAL preprint 95-021 (1995).
[30] CTEQ Collab., H.L Lai et al., Phys. Rev. D51 (1995) 4763.
[31] M. Glück, E. Reya and A. Vogt, Z. Phys. C53 (1992) 127; Phys. Lett B306 (1993) 391; DESY-94-206 (1994).
[32] A. Donnachie and P.V. Landshoff, Z. Phys. C61 (1994) 139.
[33] ZEUS Collab., M. Derrick et al., Z. Phys. C63 (1994) 391.
[34] H. Abramowicz, E.M. Levin, A. Levy, U. Maor, Phys. Lett. B269 (1991) 465.
[35] ZEUS Collab., M. Derrick et al., Phys. Lett. B315 (1993) 481.
[36] UA8 Collab., R.Bonino et al., Phys. Lett. B211 (1988) 239; UA8 Collab., A.Brandt et al., Phys. Lett. B297 (1992) 417.
[37] K. Goulianos, Nucl. Phys. B (Proc. Suppl.) 12 (1990) 110.
[38] N.N. Nikolaev and B.G. Zakharov, Z. Phys. C53 (1992) 331.
[39] POMPYT 1.0: P. Bruni and G. Ingelman (unpublished); DESY 93-187; Proceedings of the Europhysics Conference on HEP, Marseille 1993, 595.
[40] G. Ingelman and P. Schlein, Phys. Lett. 152B (1985) 256.
[41] A. Solano, Ph.D. Thesis, University of Torino 1993 (unpublished); A. Solano, Proceedings of the International Conference on Elastic and Diffractive Scattering, Nucl. Phys. B (Proc. Suppl.) 25 (1992) 274; P. Bruni et al., Proceedings of the Workshop on Physics at HERA, DESY Vol. 1 (1991) 363.
[42] J.D. Bjorken and J. Kogut, Phys. Rev. D8 (1973) 1341.
[43] H.-U. Bengtsson and T. Sjöstrand, Comp. Phys. Comm. 46 (1987) 43; T. Sjöstrand, CERN-TH 6488/92.
[44] A. Donnachie and P.V. Landshoff, Nucl. Phys. B244 (1984) 322; Phys. Lett. B191 (1987) 309; Nucl. Phys. B303 (1988) 634; Phys. Lett. B285 (1992) 172.

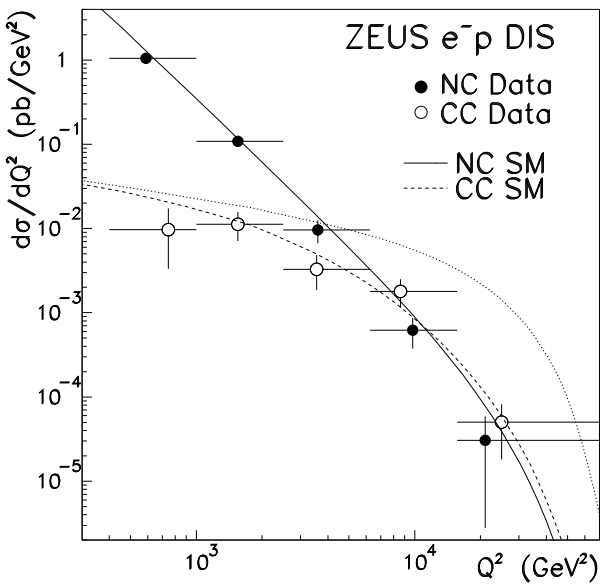

Figure 1. *Neutral current and charged current cross-sections as a function of Q^2 from the ZEUS 1993 data. The solid curve shows the Standard Model prediction for neutral currents and the dashed curve the Standard Model prediction for charged currents. The dotted curve shows the prediction for an infinite mass W.*

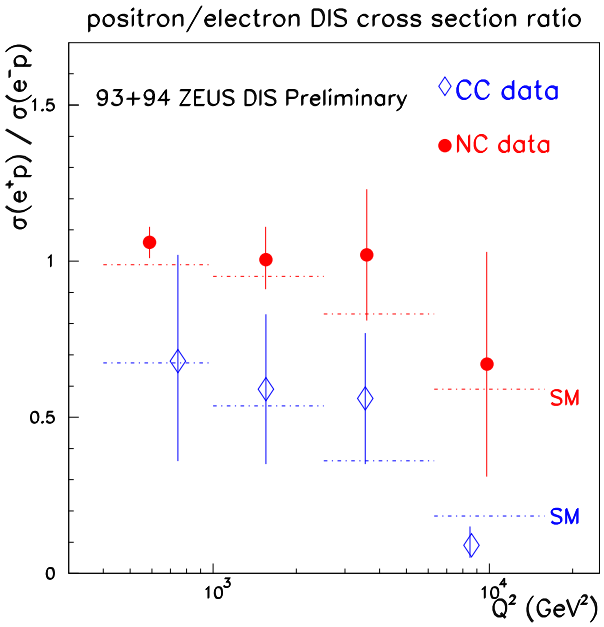

Figure 2. *Ratio of positron and electron total cross-sections as a function of Q^2. The dotted lines show the Standard Model predictions.*

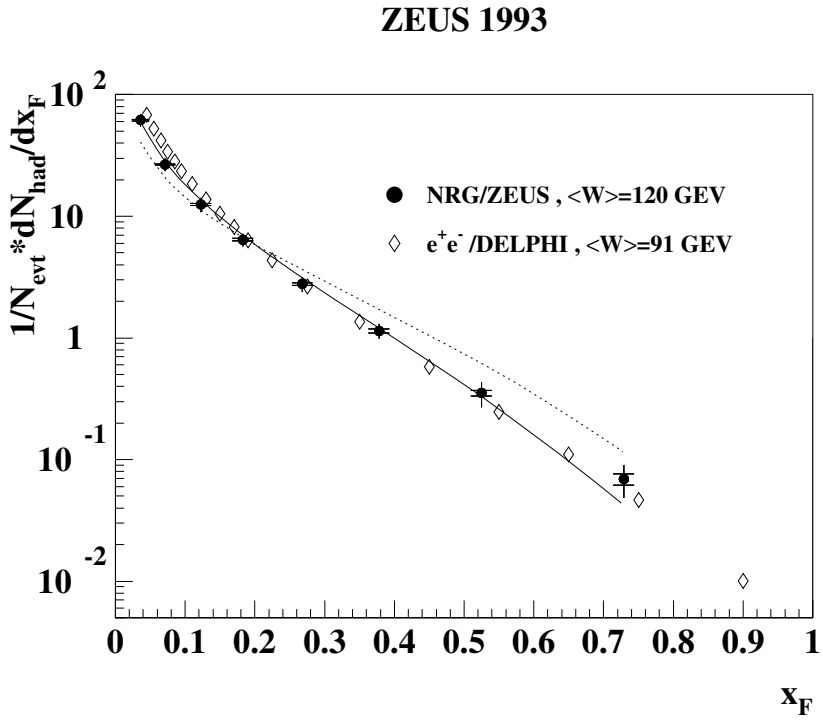

Figure 3. *Normalised x_F distributions for charged particles for the ZEUS deep inelastic scattering data together with the distributions for e^+e^- data from the DELPHI experiment [3] at similar $< W >$. The solid line is the prediction of the MEPS Monte Carlo model [4]. The dotted line is the prediction of the naive quark-parton model.*

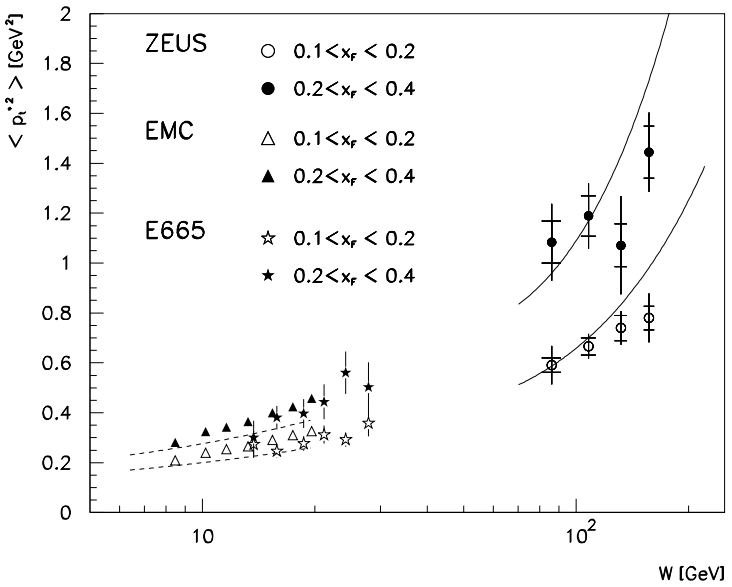

Figure 4. *$< p_T^{*2} >$ distributions in two ranges of x_F for charged particles for the ZEUS deep inelastic scattering data together with the EMC [5] and E665 [6] distributions at lower $< W >$. The solid line shows the prediction from the MEPS Monte Carlo model, the dotted line shows the prediction from a phase space model excluding the effects of hard gluon radiation.*

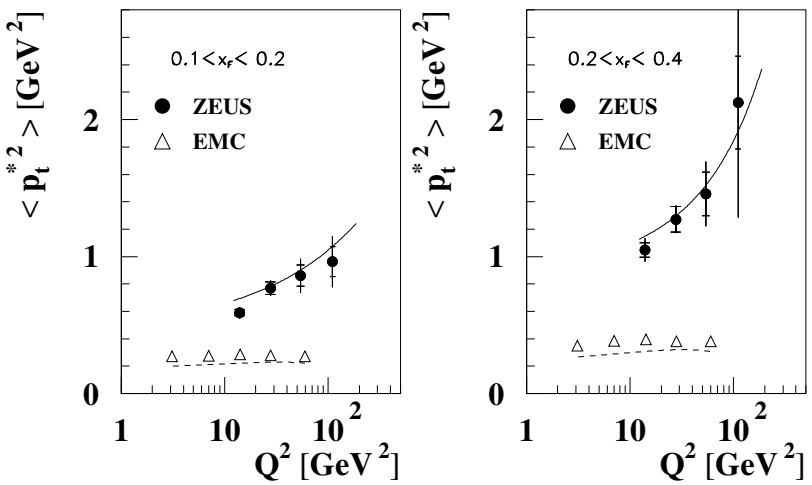

Figure 5. $< p_{\mathrm{T}}^{\star 2} >$ *distribution as a function of* Q^2 *for the ZEUS and EMC experiments for two different ranges in* x_{F}. *The solid line shows the prediction from the MEPS Monte Carlo model, the dotted line shows the prediction from a phase space model excluding the effects of hard gluon radiation.*

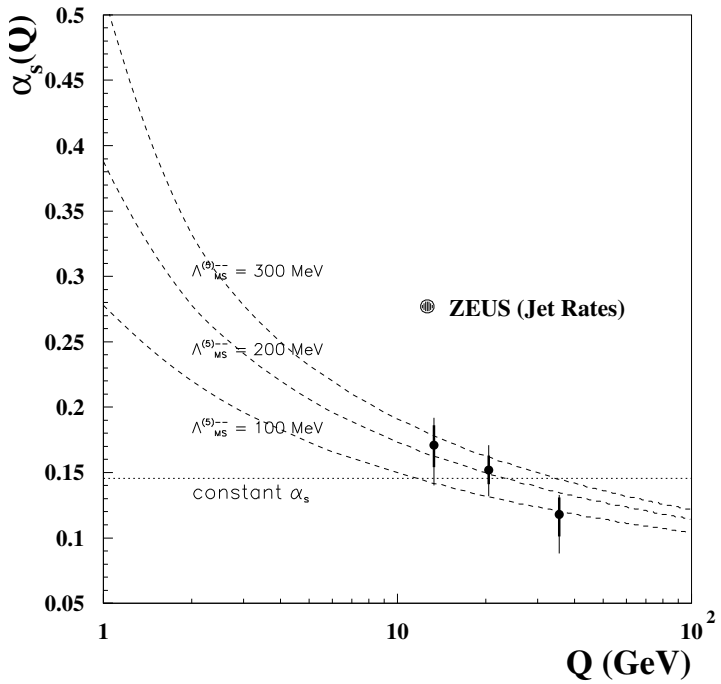

Figure 6. *Measured values of* α_s *for three different* Q *regions. The statistical and systematic errors are shown as the thick and thin vertical bars respectively. The systematic errors between the three points are strongly correlated. The dashed lines show the QCD predictions for three possible values for* $\Lambda^{(5)}_{\overline{MS}}$. *The dotted line shows the best fit to the hypothesis that* α_s *is constant.*

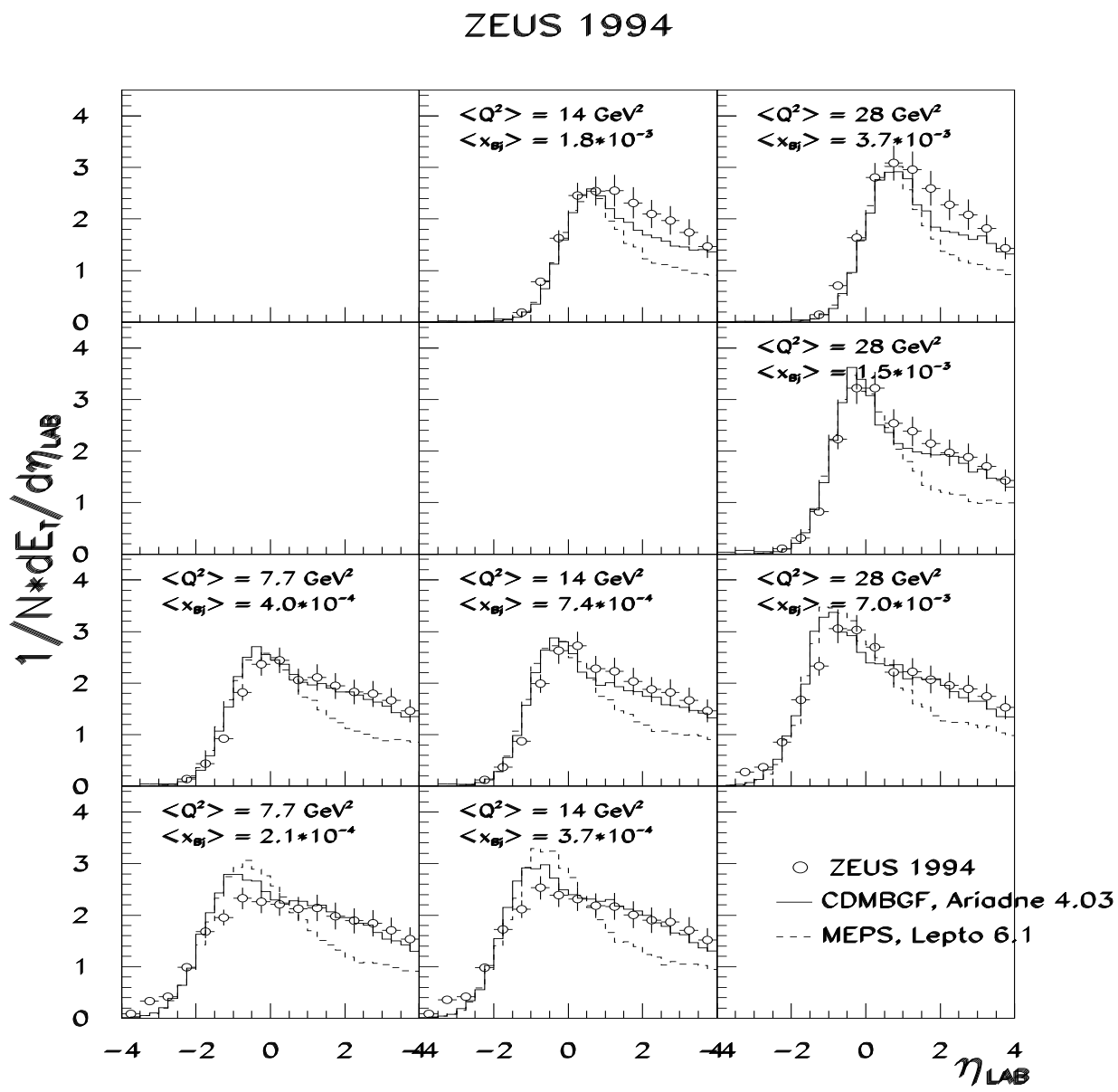

Figure 7. *The corrected normalised energy flow per unit rapidity in Q^2, x bins. Q^2 increases towards the right of the figure, x increases vertically. Also shown are predictions from the CDMBGF model as implemented in ARIADNE 4.03 (solid line) and the MEPS model as implemented in LEPTO 6.1 (dashed line).*

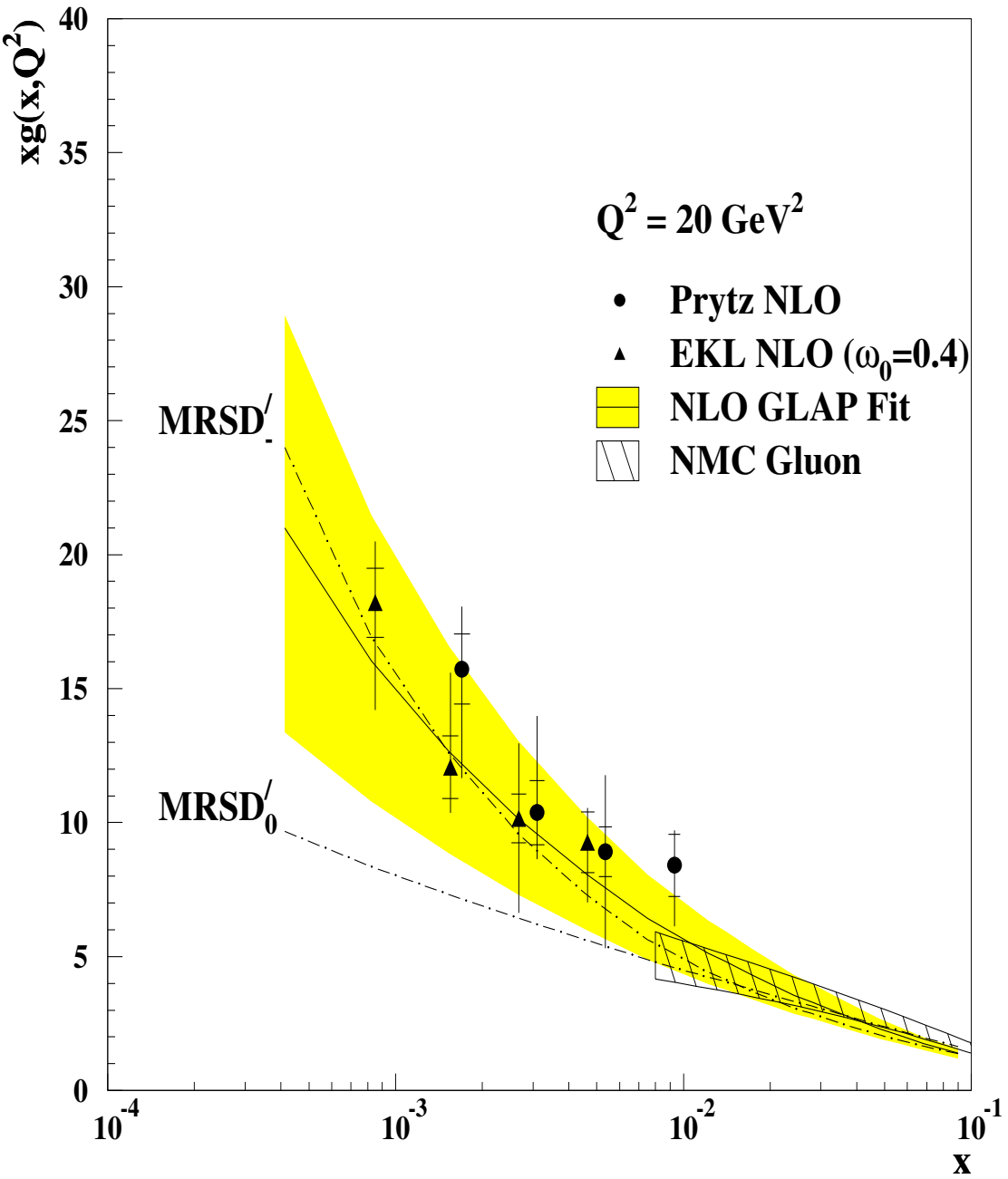

Figure 8. *$xg(x)$ as a function of x as determined from scaling violations in the 1993 ZEUS F_2 data. Two approximate determinations from Prytz and Ellis, Kunszt and Levin are shown. The angled shaded region shows a determination at higher x from the NMC experiment. The shaded region shows the full QCD fit to the ZEUS 1993 data. Also shown as dashed-dotted lines are the $MRSD'_0$ and $MRSD'_-$ parameterisations of $G(x)$ [15].*

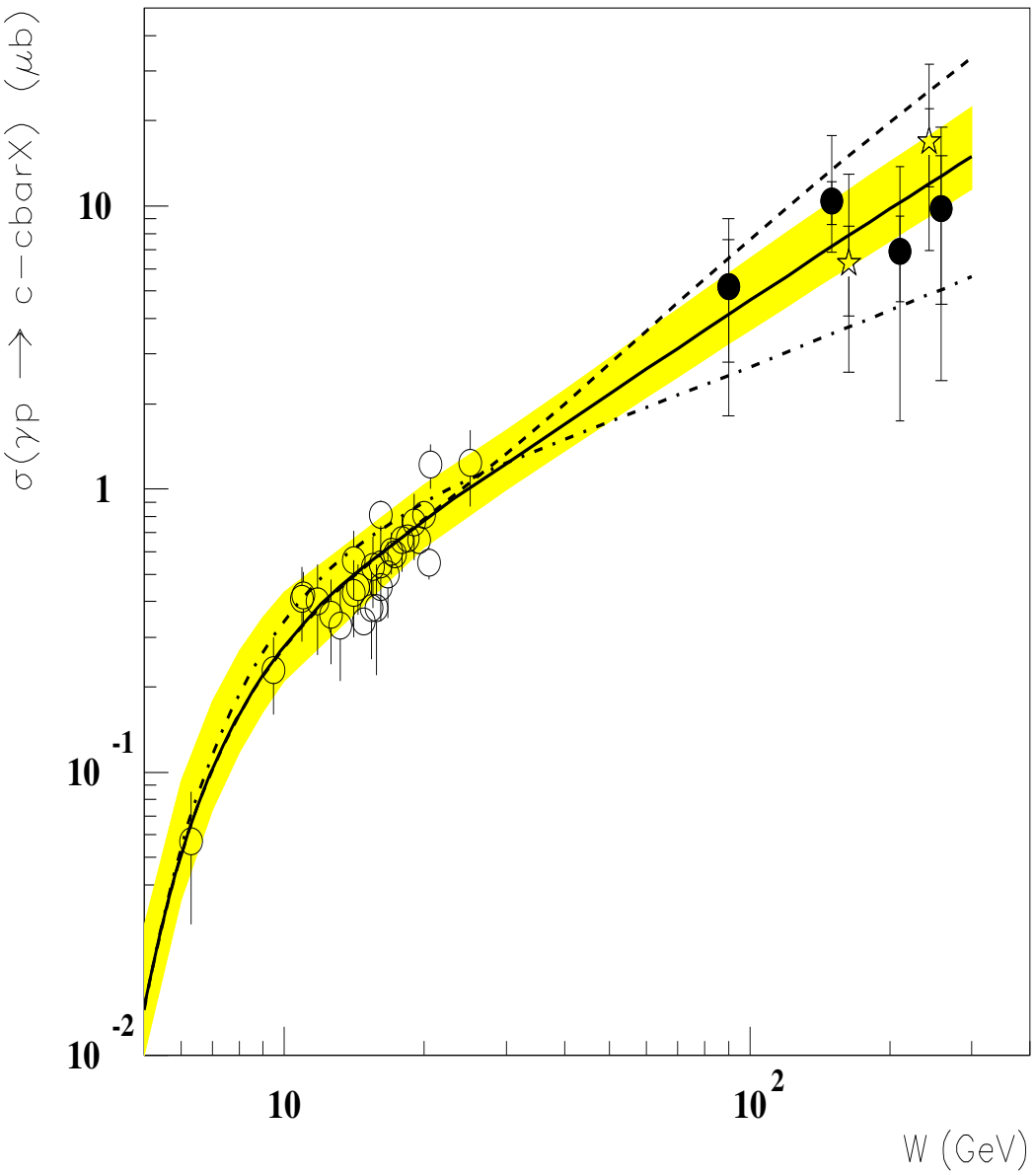

Figure 9. *The cross-section for total charm photoproduction as a function of W. The starred data points show the ZEUS results derived from the observation of inclusive $D^\star$ mesons, while the solid points are derived from the isolation of inclusive high $p_{\rm T}$ muons. The open circles show data from fixed-target experiments [17]. The solid line shows the predictions of the model by Frixone et al, based on the $MRSD'_$ and GRV(HO) [18] structure functions for the proton and photon respectively. The shaded area shows the uncertainty due to renormalisation scale. The higher dotted line shows similar predictions based on $MRSD'_$ and LAC1 [19], while the lower dotted line is based on $MRSD_0$ and GRV(HO).*

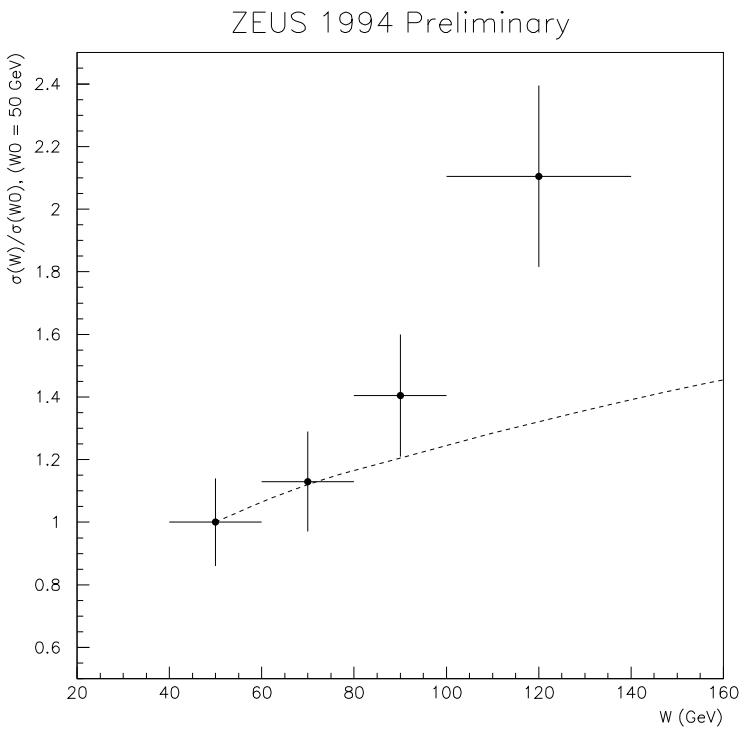

Figure 10. *The relative J/ψ cross-section as a function of W from preliminary 1994 data. The relative cross-section is shown normalised to the point at $W = 50$ GeV. A steep rise of the cross-section with W is observed. The dotted line shows the prediction of the model of Donnachie and Landshoff [24].*

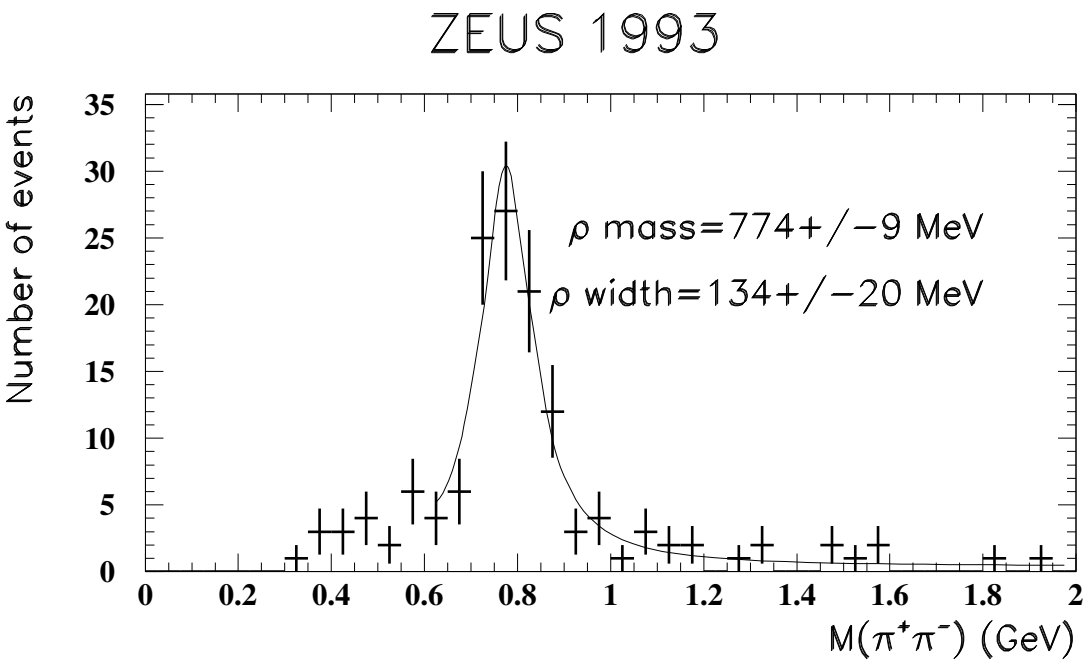

Figure 11. *The $\pi^+\pi^-$ invariant mass distribution for ρ candidates in deep inelastic scattering for $7 < Q^2 < 25$ GeV^2 and $40 < W < 130$ GeV.*

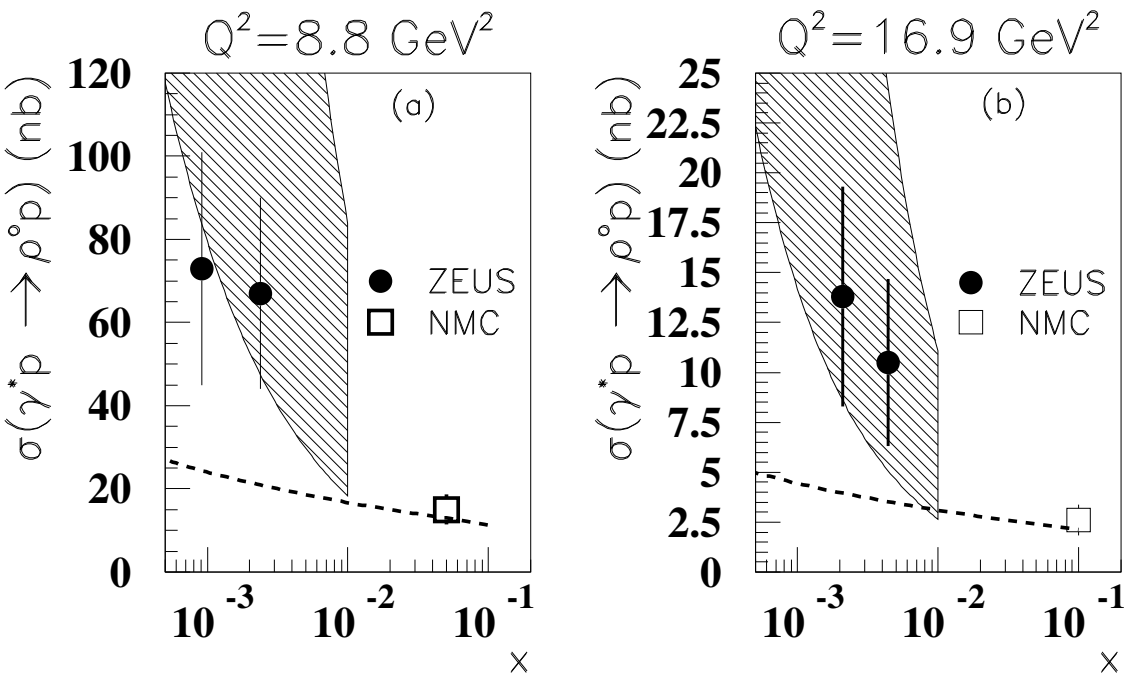

Figure 12. *a)$\sigma(\gamma^* p \to \rho^o p)$, as a function of x at $Q^2 = 8.8\ GeV^2$. The errors shown include both statistical and systematic uncertainties added in quadrature. Also shown is the NMC result[25]. The dashed curve is a prediction from [26]. The hatched area corresponds to the predictions of Brodsky et al. [22] for $x < 0.01$, where the upper and lower limits are obtained from the limits on $xg(x)$ from [11]. b) a similar plot for data at $Q^2 = 16.9\ GeV^2$.*

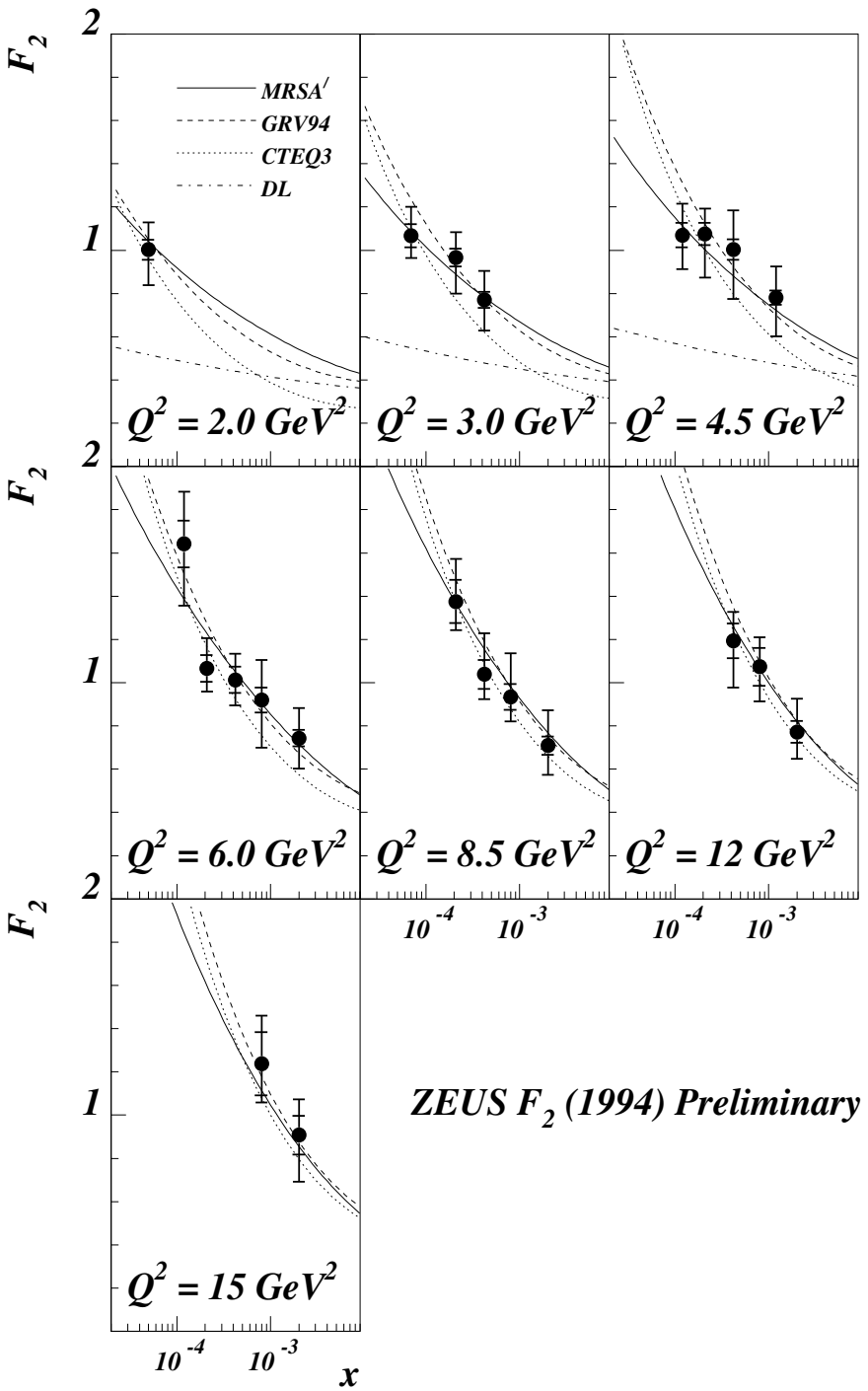

Figure 13. *Values of F_2 in selected Q^2 intervals as determined from the 1994 ZEUS data sample taken with a vertex shifted by 67 cm from the nominal position in the incoming proton direction Also shown are the latest parameterisations from MRS [29], CTEQ [30] and GRV [31] as well as the Regge-inspired prediction of Donnachie and Landshoff [32].*

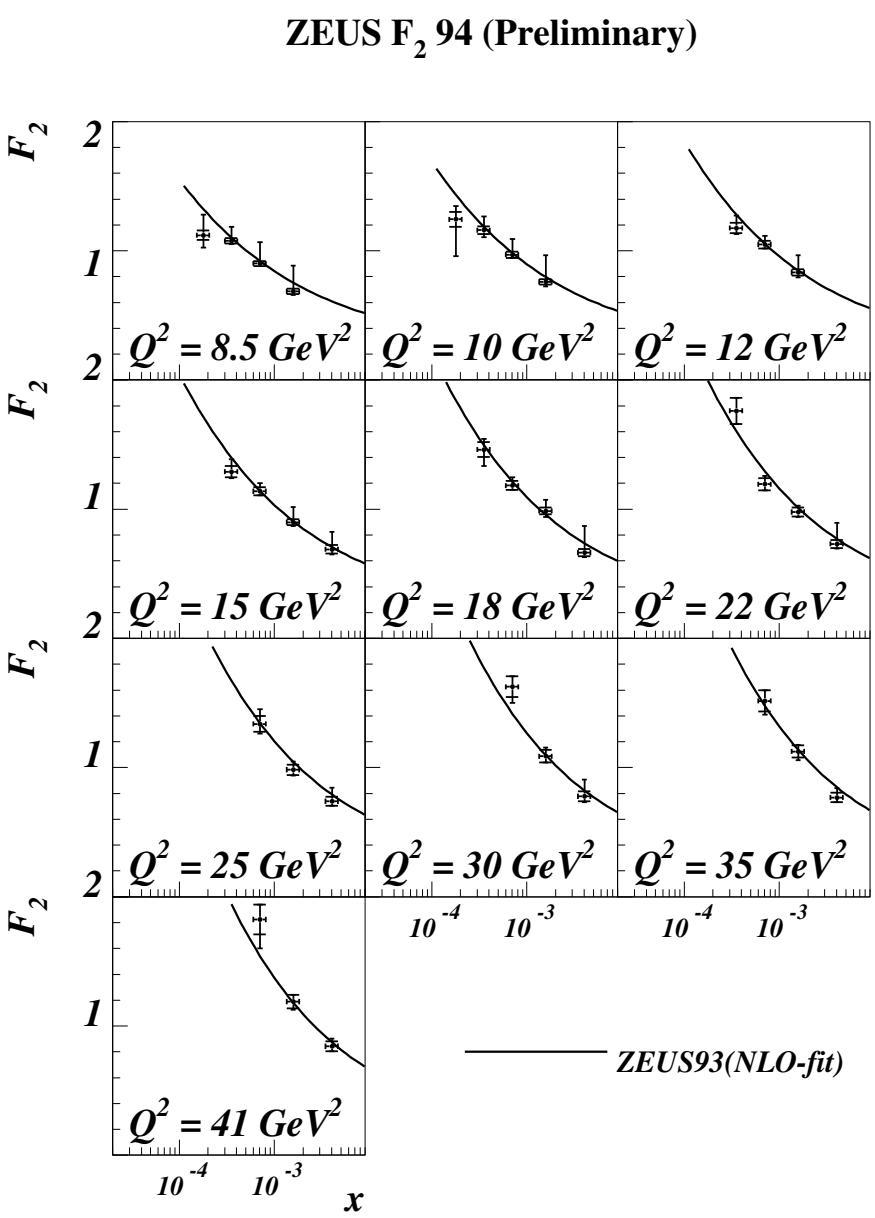

Figure 14. *Values of F_2 in selected Q^2 intervals as determined from the 1994 ZEUS data sample at the nominal vertex position using the DA method. The solid curve shows the QCD fit to the ZEUS 1993 data points.*

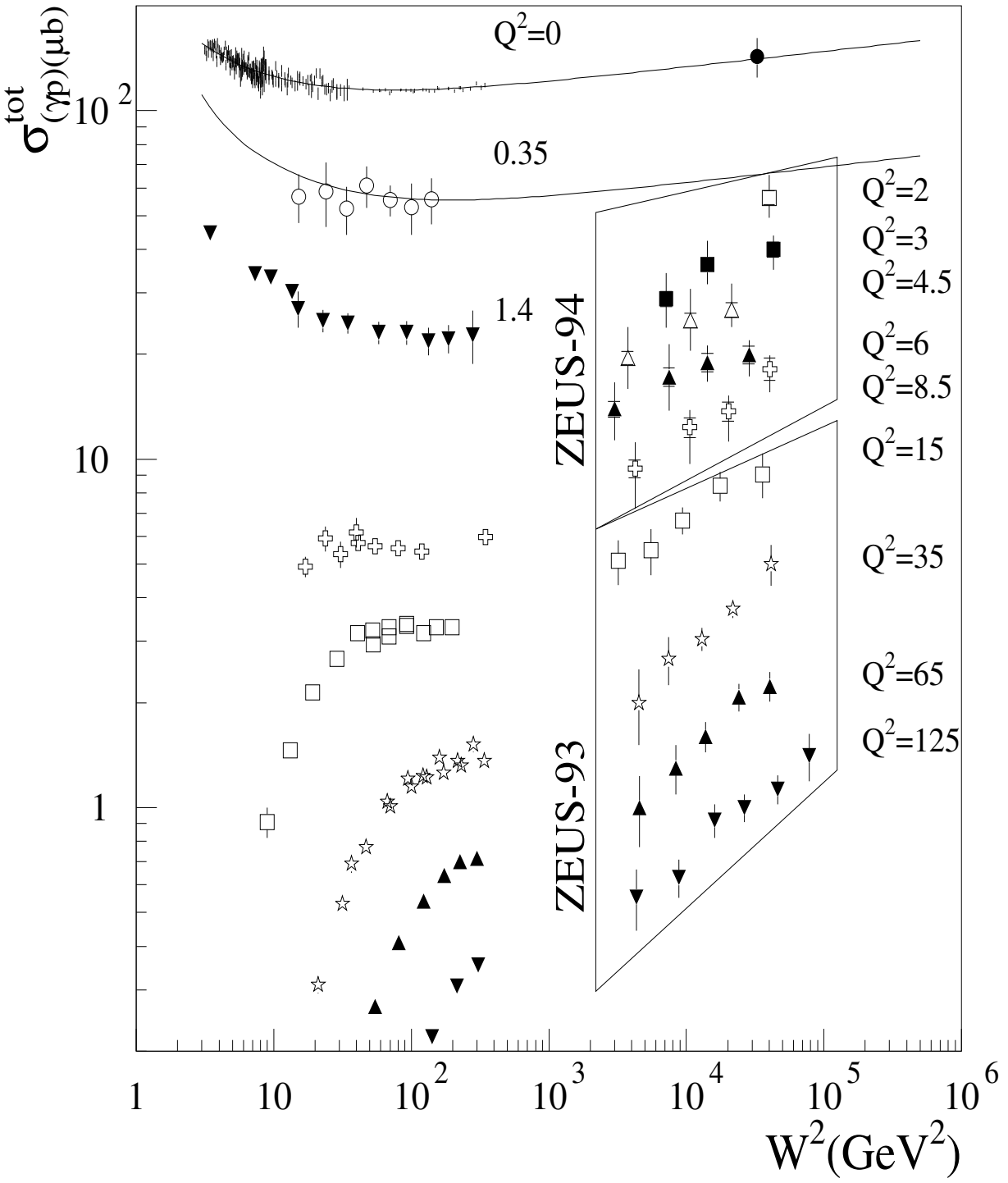

Figure 15. *Values of the total virtual photon-proton cross-section for various Q^2 (in GeV^2). The point at high W^2 and $Q^2 = 0$ is obtained from the total photoproduction cross-section measurement of ZEUS [33]. The remaining points at low W^2 are taken from a variety of fixed target experiments. The solid lines are parameterisations from Abramowicz et al. [34].*

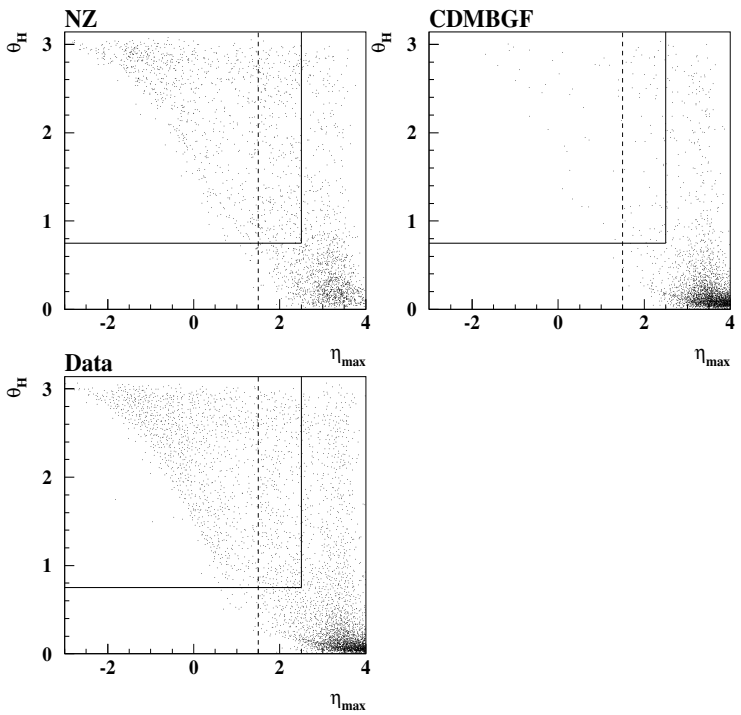

Figure 16. *Plots of θ_H and $\eta_{\max}$ for the Nikolaev-Zakharov[38] model for diffractive DIS, the CDMBGF [10] model for non-diffractive DIS, and for the ZEUS data. The solid lines show the cuts described in the text to isolate diffractive events.*

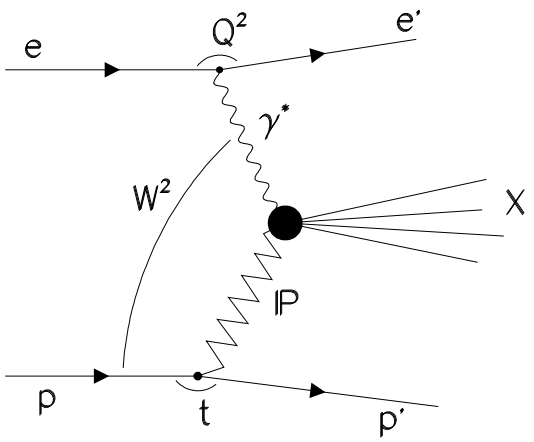

Figure 17. *Diagram of a diffractive event.*

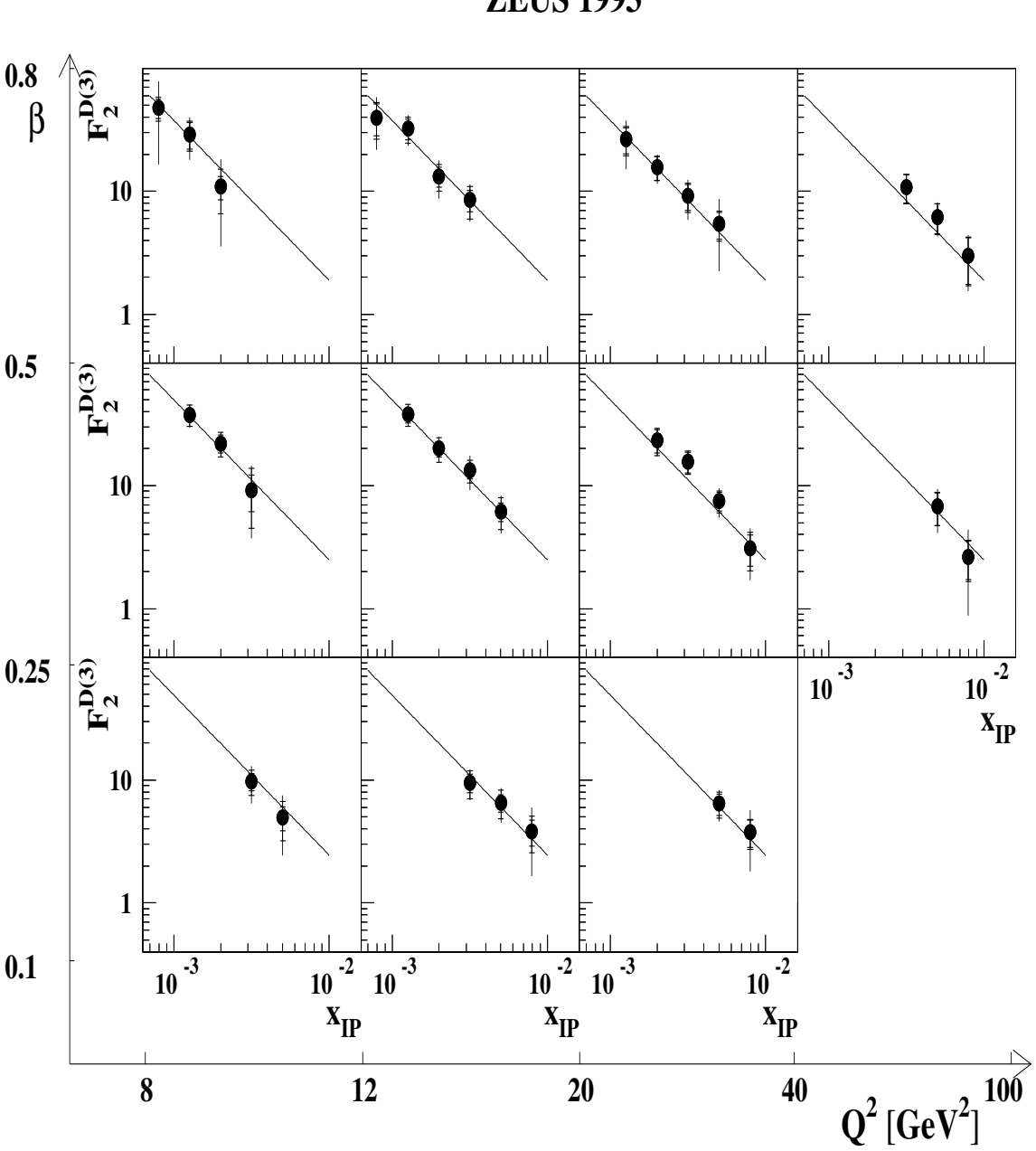

Figure 18. *The diffractive structure function. The inner error bars show the statistical errors, the outer bars correspond to the statistical errors and the DIS event selection systematic errors added in quadrature and the full line corresponds to the statistical and full systematic errors added in quadrature. The data include an estimated 15% contribution from double dissociation. The overall luminosity uncertainty of 3.5% is not included in the error bars. The solid lines are a fit to a functional form described in the text.*

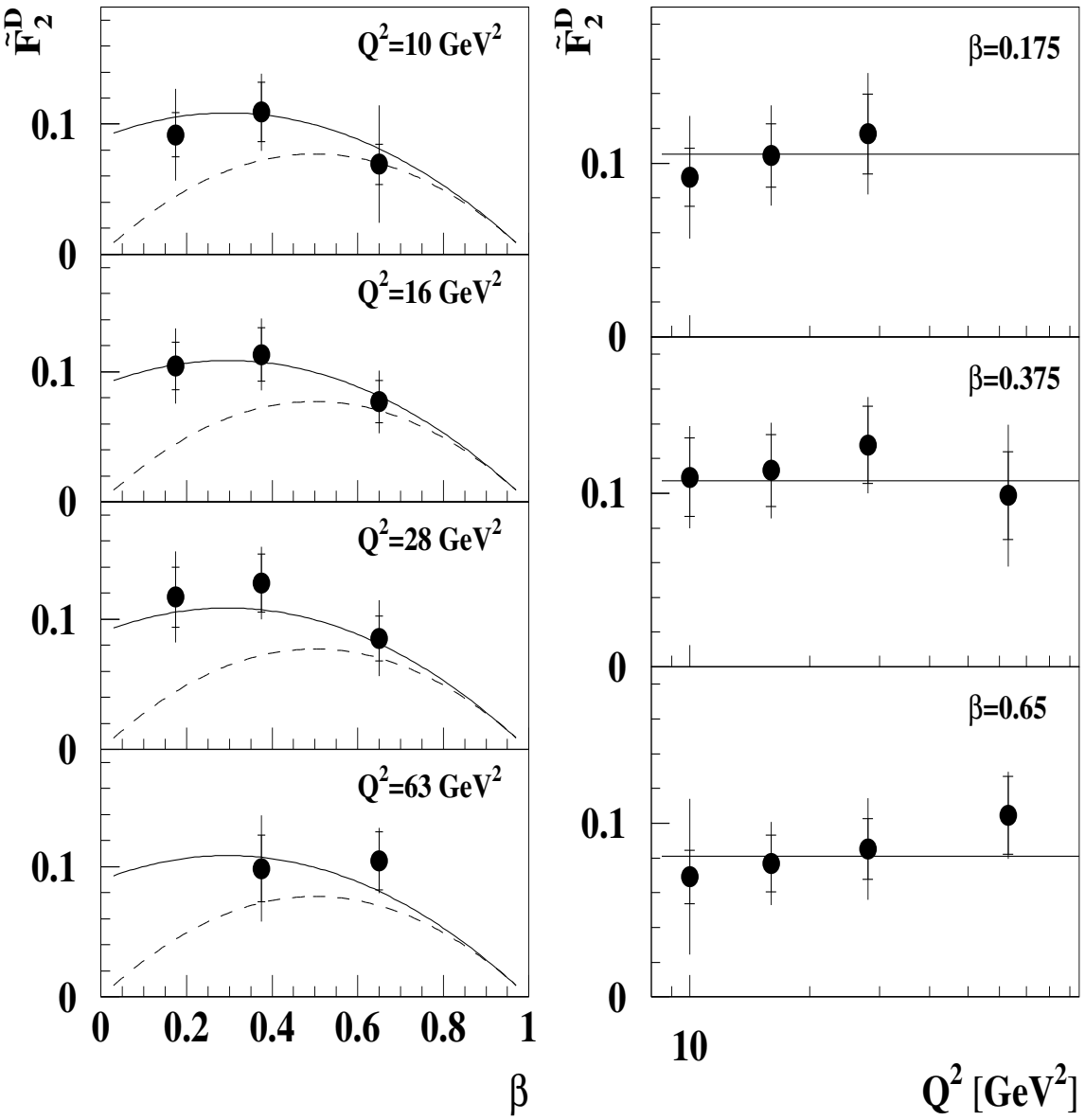

Figure 19. *The diffractive structure function integrated over $x_{I\!P}$, $\tilde{F}_2^D$. The left hand plots show the data binned in four Q^2 bins and plotted as a function of β. The right hand plots show the data in β bins and plotted as a function of Q^2. The solid line shows the prediction from the parameterisation of (9) while the dotted line shows the prediction with the soft part of that equation omitted.*

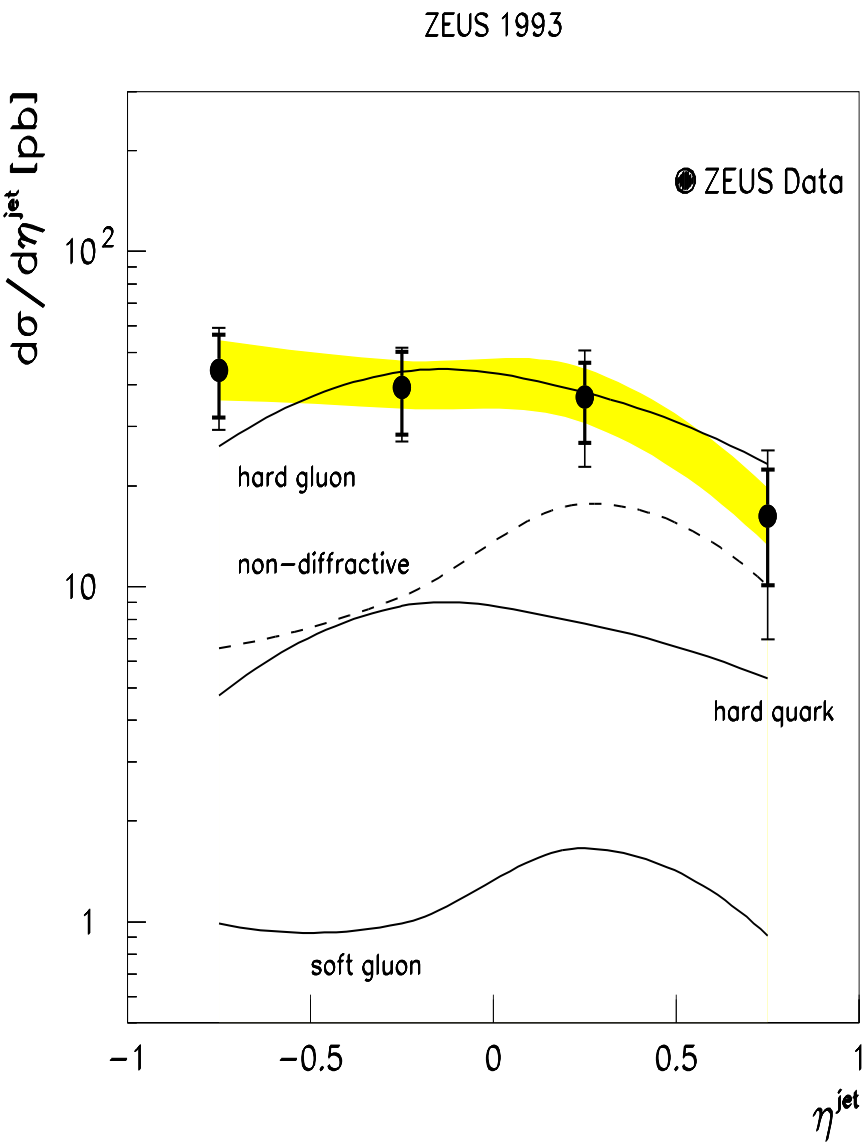

Figure 20. *Differential ep cross-section for inclusive jet production with* $\eta_{max}^{had} < 1.8$ *and* $E_T^{jet} > 8$ *GeV with* $Q^2 < 4$ *GeV*^{2} *and* $0.2 < y < 0.85$. *The inner error bars represent the statistical errors, the outer error bars the statistical and systematic errors added in quadrature, excluding the uncertainty on the energy scale of the jets, which is shown separately as the shaded band. The solid lines show the predictions of representative models of diffractive processes with various parameterisations of the parton content of the pomeron. The dotted line shows an example of the contribution from non-diffractive processes from the PYTHIA Monte Carlo [43].*

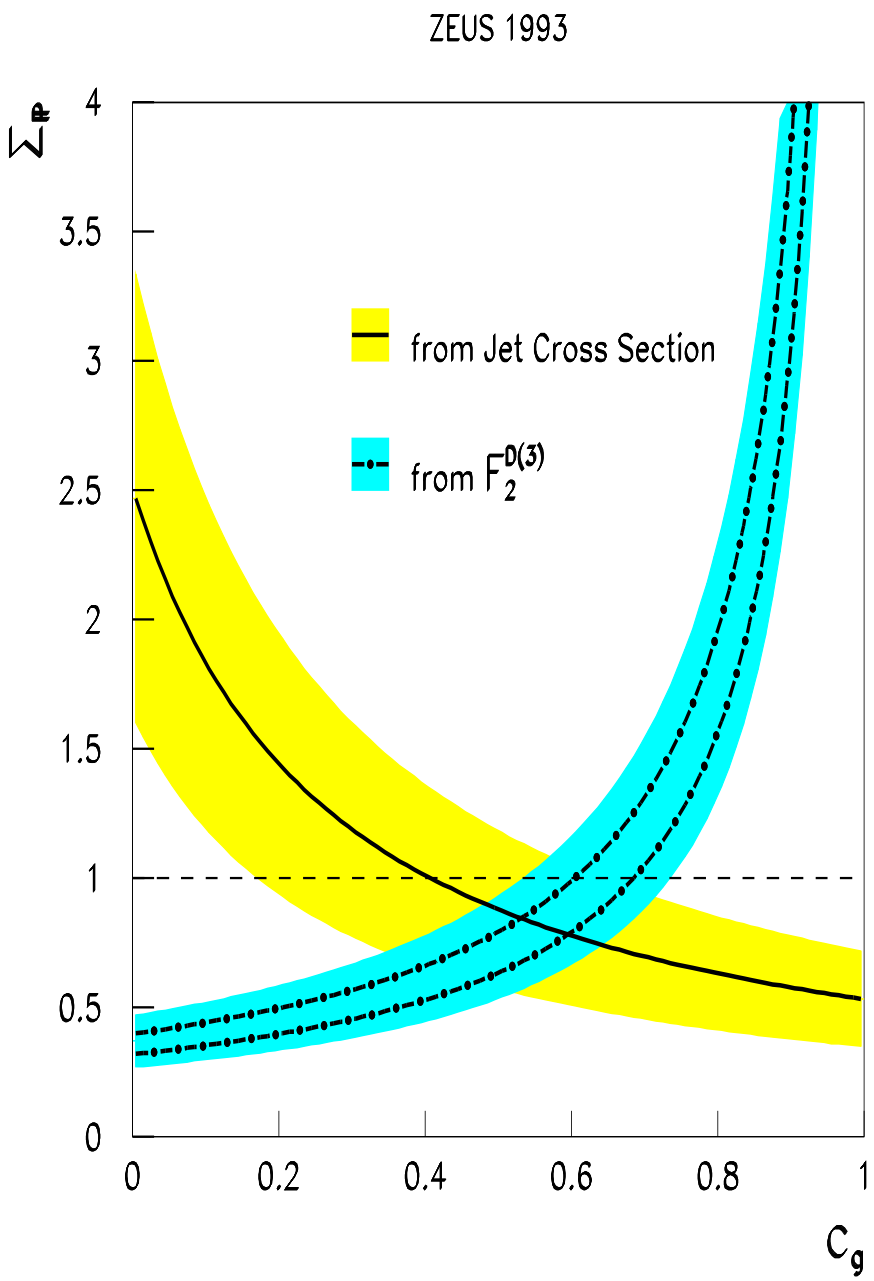

Figure 21. *$\Sigma_{I\!P}$ against c_g. The solid line represents the χ^2 minimum and the shaded band the 1σ limits for the fit to the hard photoproduction jet cross-section. The data from the diffractive DIS structure function is represented by the dashed-dotted lines for the two choices of the number of contributing quark flavours and the shaded area is the 1σ error band.*